

# 6–100 GHz research progress and challenges from a channel perspective for fifth generation (5G) and future wireless communication

Jianhua ZHANG<sup>1\*</sup>, Pan TANG<sup>1</sup>, Lei TIAN<sup>1</sup>, Zhixue HU<sup>1</sup>,  
Tan WANG<sup>2</sup> & Haiming WANG<sup>3</sup>

<sup>1</sup>State Key Laboratory of Networking and Switching Technology,  
Beijing University of Posts and Telecommunications, Beijing 100876, Beijing;

<sup>2</sup>State Radio Monitoring Center of China, Beijing 100037, China;

<sup>3</sup>State Key Laboratory of Millimeter Waves, Southeast University, Nanjing 210096, China

Received December 31, 2016; accepted June 6, 2017; published online June 30, 2017

**Abstract** Radio frequency is a valuable resource for wireless communication systems. The high-frequency band from 6 GHz up to 100 GHz, where continuous and broad spectra exist, is promising to meet the high spectrum requirement of fifth generation (5G) mobile communication systems by 2020. To date, many groups from academia and industry have contributed to devising approaches to allocate and utilize frequency resources from 6 GHz to 100 GHz for 5G and future wireless communication systems. In this paper, we present global efforts to allocate potential frequency bands and field trial progress from 6 GHz to 100 GHz for 5G. From a channel perspective, we summarize research progress and challenges, including channel measurement platforms and channel parameter analysis, both of which are important to extract the inherent channel characteristics and use a high-frequency band for 5G and future wireless communication systems.

**Keywords** 5G, high frequency band, millimeter wave, channel, measurement

**Citation** Zhang J H, Tang P, Tian L, et al. 6–100 GHz research progress and challenges from a channel perspective for fifth generation (5G) and future wireless communication. *Sci China Inf Sci*, 2017, 60(8): 080301, doi: 10.1007/s11432-016-9144-x

## 1 Introduction

The global mobile service is currently experiencing exploratory development, and it is likely to continue growing steadily. Moreover, the emergence of ultra-high-definition video, mobile cloud computing, and other high-quality data services can definitively be expected to contribute to enormous growth in the mobile services. To address the rapid expansion of mobile data services, various countries and regions have set up fifth generation (5G) research committees or groups, e.g., the Mobile and Wireless Communications Enablers for the Twenty-Twenty (2020) Information Society (METIS) in Europe, the International Mobile Telecommunication for 2020 (IMT-2020) and IMT-2020 (5G) Promotion Group in

\* Corresponding author (email: jhzhang@bupt.edu.cn)

China, the 5G Forum in South Korea, and 2020 and Beyond Ad-hoc in Japan. According to the International Telecommunications Union-Radiocommunication (ITU-R) IMT Vision [1], three typical usage scenarios have been defined for 5G, namely enhanced mobile broadband (eMBB) such as wide coverage and hotspots, ultra-reliable and low-latency communications (uRLLC) such as self-driving vehicles, and massive machine-type communication (mMTC) such as the smart city-home. The key targets of IMT-2020 are: a peak data rate of 20 Gbps, user-experienced data rate of 100 Mbps, and latency of 1 ms. Three possible ways in which to meet the demand of future mobile data growth exist: a) improving the spectral efficiency, e.g., employing massive multiple-input multiple-output (MIMO) [2]; b) splitting into smaller cells, e.g., ultra-densification networks (UDN); and c) finding additional radio spectrum.

However, wide-band spectrum is only available at frequencies above 6 GHz. At the World Radio Conference 2015 (WRC-15), the possibility of using a frequency band above 6 GHz for IMT was discussed and some frequency bands were considered as future potential candidate IMT bands, such as 24.25–27.5 GHz, 37–40.5 GHz, 42.5–43.5 GHz, 45.5–47 GHz, 47.2–50.2 GHz, 50.4–52.6 GHz, 66–76 GHz, and 81–86 GHz. Further, 31.8–33.4 GHz, 40.5–42.5 GHz, and 47–47.2 GHz may be additionally allocated to the mobile service on a primary basis. The Federal Communications Commission (FCC) adopted new rules to create a new Upper Microwave Flexible Use service at 28 GHz (27.5–28.35 GHz) on July 14, 2016. The 5G technology research and development trial mainly consists two parts: a technology scheme trial and a system trial. Many companies in the world participate in promoting the development of 5G key technologies and supporting the global unified 5G standardization by contributing to the trial, such as Huawei, Ericsson, Qualcomm, Samsung, and Google. In China, the results of the first stage of the key technology trial were released on September 22, 2016. For example, the maximum cell throughput of multiple-user MIMO (MU-MIMO) is more than eight times that of single-user MIMO (SU-MIMO) with two streams. The peak data rates can reach 27 Gbps and 15 Gbps at 73 GHz and 15 GHz, respectively.

The channel characteristics are the foundation to the technology research and system trial. Taking full advantage of high frequency to mobile communication necessitates a comprehensive understanding of high-frequency channel propagation characteristics. However, as the frequency increases, the radio propagation mechanism changes [3] and some channel characteristics, e.g., path loss, delay spread and angle spread, are a function of frequency [4]. In addition, rain attenuation and atmospheric attenuation affect the propagation of high-frequency signals [5, 6]. The most direct and effective way to obtain these channel characteristics is to conduct wireless propagation channel measurements by specially designed equipment [7]. New York University (NYU) in the USA, the Tokyo Institute of Technology in Japan, Beijing University of Posts and Telecommunication (BUPT) and Southeast University (SEU) in China, Aalto University in Finland, etc., have conducted experimental measurements of the high-frequency channel. Their work covers various frequencies, scenarios, and channel characteristic parameters, e.g., path loss, K-factor, delay spread, and angle spread, using a platform based on either a vector network analyzer (VNA-based) or discrete components (DC-based) [8–14]. Their work contributes to the realization of channel model standardization in the form of the 3rd Generation Partnership Project (3GPP) technical report (TR) 38.900 [4]. This standardization lists the statistics of key parameters of the 6–100 GHz frequency channel. In terms of the measurement hardware there are mainly two types of high-frequency measurement platforms. The first type of platform is based on a vector network analyzer (VNA) [12], which extracts channel information over the frequency domain. The main advantage of this platform is that it can work at a wide central frequency and realize time synchronization easily, whereas its disadvantage is that the measured distance is limited because the signals at the transmitter (TX) and receiver (RX) are collected together. Another type of platform is established using discrete components, including a signal generator, signal receiver, converter, and amplifier. Although the transmitter side and receiver side of this platform are separated, which removes the limitation of the measured distance, it introduces the problem of time synchronization between TX and RX. Conducting MIMO measurements successfully and obtaining precise channel information indeed requires a reliable method for synchronizing the clock signal of TX and RX. Ref. [15] proposes a time synchronization technique that generates time stamps of the transmitting time on each measurement such that all measurements are aligned with the corresponding relative transmitting time. On the other hand, different types of antennas influence the analysis results

in different ways. For example, a horn antenna would detect a narrower version than an omnidirectional antenna. Correspondingly, a horn antenna would receive fewer multipath components. Furthermore, for a MIMO measurement, antenna arrays are needed to create a spatial difference between adjacent antennas, as this would enable us to use the Spatial space-alternating generalized expectation-maximization (SAGE) algorithm to extract the spatial characteristics [16]. Virtual measurements by rotating the horn antenna is another method to obtain the spatial characteristics [17]. However, the selection of the size of the rotating step, which affects the virtual antenna pattern, is inconclusive. Generally, because of the limitation of the measurement platform, measurements in the high-frequency band do not have mobility. Hence, there is no time variance in the measured data. If we use the data to calculate the K-factor, which is the power ratio between the line-of-sight (LoS) component and scattered components [18], with the traditional method [19], the K-factor we obtain only reflects the variance of the surrounding moving vehicles or people rather than the channel fading. Thus, a new method is necessary to calculate the K-factor from the measured data without mobility. In terms of the channel model, the channel dimensions have been continuously expanded from the time domain to the three domains of space, time, and frequency in the last few decades, which means that the channel properties are deeply explored. In [20], we proposed a one-nuclei-based channel model, which takes advantage of big data and machine-learning techniques for wireless channel modeling, to combine the stochastic and deterministic models. The model solves the acquisition of map information by using a machine-learning algorithm and is therefore promising for future wireless communication, and worthy of further study.

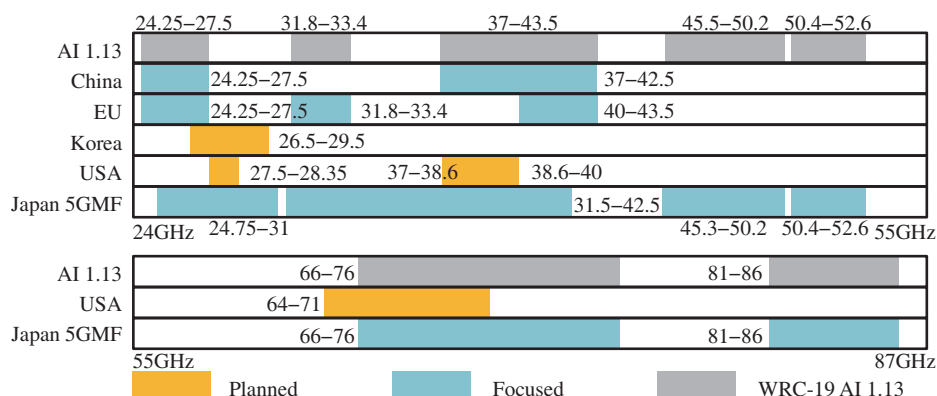
In this paper, we review research progress in the 6–100 GHz frequency band and point out the challenges presented by each related aspect. First, the frequency requirements and current field trials in the world are introduced, after which the research progress and challenges relating to the 6–100 GHz frequency band are mainly discussed, including channel measurement platforms and channel parameter analysis.

## 2 Potential global high-frequency bands

Owing to low propagation loss, frequencies below 6 GHz are quite popular and have been allocated to a variety of traditional services that coexist below the tolerable interference level. Likewise, spectrum planning and candidate high-frequency bands for mobile communication should also ensure that all the services can perform well simultaneously, and the proposal of future 5G potential bands should be based on this premise. Figure 1 shows the potential bands above 6 GHz surveyed from the public sources in four major regions in the world, i.e., the Ministry of Industry and Information Technology (MIIT) in China, Conference Europe of Post and Telecommunications (CEPT) in the European Union (EU), Korea Communications Commission (KCC) in Korea, FCC in the USA, and the 5G Mobile Communications Promotion Forum (5GMF) in Japan. The candidate bands that will be discussed under WRC-19 Agenda Item (AI) 1.13 are also listed there. Below we further discuss the details about choosing these potential bands in three main countries and organizations in the world.

### 2.1 China

At the 2nd 5G Global Summit in Nov. 2016 in Italy, an official elaboration was made on 5G high-frequency bands considered by the Bureau of Radio Regulation of the MIIT of China. Basically, China plans to promote global/regional harmonization under WRC-19 AI 1.13 and plans to give high priority to the 20–40 GHz band for outdoor deployment. Currently, as shown in Figure 1, China is focusing on compatibility studies of the 26 GHz (25.25–27 GHz) and 40 GHz (37–42.5 GHz) bands. In the frequency allocation table of China, the situation of these two bands is complicated with inter-satellite services, space research services, fixed satellite services and so on, as the primary services. Yet, it is vital to take care of the existing usage of these services and further research, including channel models and system models, is required.



**Figure 1** The potential high-frequency bands surveyed by China, the EU, Korea, the USA, and Japan and the candidate bands are scheduled to be discussed in WRC-19 AI 1.13. “Planned” means there are plans to use these frequency bands; “Focused” means mainly these frequency bands are considered; “WRC-19 AI 1.13” means these are the candidate bands scheduled for discussion at the WRC-19 meeting.

## 2.2 Europe

In November 2016, the radio spectrum policy group (RSPG) in Brussels drafted a strategic roadmap towards 5G for Europe [21], which presents their opinion on spectrum-related aspects for 5G and aims to facilitate the launch of 5G on a large scale by 2020. Since it remains necessary to utilize 24 GHz to ensure all the performance targets of 5G, the consideration focuses on the three bands shown in Figure 1 to strengthen the global harmonization opportunities. The reasons for supporting the 24.25–27.5 GHz band are the large bandwidth of more than 3 GHz and the possibility for equipment to support a continuous tuning range with the 28 GHz band in order to facilitate economies of scale within the USA and Korea. In addition, the possibility to leverage the ongoing development for other markets is also deemed to lower the implementation risks and allow for early access to equipment.

RSPG recognizes that the 31.8–33.4 GHz band appears to be a promising and could be made available relatively easily by many European administrations, taking into account the existing fixed service deployment in this band, for future deployment of 5G services. However, this frequency band would need to be studied further to assess its future availability, the demand from industry, the potential for global harmonization and the required technical conditions to protect existing services. The majority of the responses from the satellite sector support the 32 GHz band as the pioneer band. The main reasons are the low current use and the fact that the band was proposed as a candidate band by all regions at WRC 15, therefore making it a good candidate for global harmonization. RSPG considers the 0.5–43.5 GHz band to be a viable option for 5G in the longer term, taking into consideration the support from mobile industry and the need to take into consideration the general balance between the mobile and satellite sector to access the 40/50 GHz range.

## 2.3 USA

The US selected to move fast to establish leadership in 5G by becoming the first country in the world to open high-band spectrum for 5G networks and technologies. Soon, a total of 10.85 GHz of spectrum resource will be released as shown in Figure 1. On the other hand, to continue to dramatically increase the spectrum available for next generation services, an additional 18 GHz spectrum was proposed for consideration: 24–25 GHz (24.25–24.45/24.75–25.25 GHz), 32 GHz (31.8–33.4 GHz), 42 GHz (42–42.55 GHz), 51 GHz (50.4–52.6 GHz), 70 GHz (71–76 GHz), and 80 GHz (81–86 GHz). Moreover, the spectrum above 95 GHz is also being considered.

In conclusion, although a substantial amount of bandwidth is available in the high-frequency band above 6 GHz, different regions or countries have their own spectrum allocation policies that vary considerably. Thus, to support long-term growth in the industry, it is important to globally achieve a uniform spectrum allocation policy that corresponds to the overall interests. Furthermore, it would be necessary

to allocate continuous wide bandwidth to satisfy the spectrum demand of 5G. Finding some common wide bandwidth for 5G presents an even larger problem and would require negotiation among the various interested entities. Fortunately, there has been global consensus to formulate a uniform 5G standard.

Lastly, the propagation characteristics of high-frequency signals should be considered when determining how to assign spectrum resources for 5G. According to the Friis free space path loss formula, with a certain transmitter and receiver distance, the higher the frequency, the larger the path loss, which in turn results in smaller coverage compared with frequencies below 6 GHz. Consequently, it is essential to investigate its propagation characteristics and understand its properties before applying these candidate bands to 5G.

### 3 Overview of chip development and field trials in the millimeter wave band

The tight time schedule for 5G deployment prompted 3GPP to draft a technical report, 3GPP TR 38.900 [4] with the intention of properly modeling and evaluating the performance of physical-layer techniques using the above-6GHz channel model. However, in order to implement 5G services by 2020, it remains urgent to plan and perform practical technical verification early and accelerate technical study.

In terms of chipsets, chipmakers have published announcements on the technology enabling the next generation of chipsets, such as the Snapdragon 835 by Qualcomm, the Helio X30 from MediaTek, and the Samsung Exynos 8895. Qualcomm announced its Snapdragon X50 5G modem platform in October 2016. It is designed to support download speeds of up to 5 Gbit/s, initially using wide bandwidths in the millimeter wave band. In addition, it can connect using a bandwidth up to 800 MHz via  $8 \times 100$  MHz carrier aggregation. By using advanced MIMO techniques such as adaptive beam-forming and beam-tracking, the Snapdragon X50 5G modem can extend the range of millimeter wave transmissions to non-line-of-sight scenarios, and supports mobility. Intel announced its 5G modem at CES 2017 in Las Vegas, calling it a “milestone for the industry” as it will allow companies to develop and launch 5G solutions earlier than previously anticipated. According to what Intel presented, the modem could support speeds exceeding 5 Gbps and ultra-low latency and its single chip supports both millimeter wave and sub-6GHz spectrum bands, incorporating massive MIMO, beam-forming technology, and advanced channel coding. Samsung also announced one of the processors that will almost certainly be launched in the Galaxy S8. The company officially provided details on the Exynos 9 Series 8895 chip. It is expected to be deployed in the Galaxy S8 and Galaxy S8 Plus. Similar to the Snapdragon 835, the Exynos 9 Series 8895 chip supports gigabit LTE networks, which are some of the fastest 5G wireless networks. The chip is also expected to improve virtual reality (VR) and support playing 4K ultra-high-definition (UHD) video at 120 fps and more.

On the other hand, 5G has not been a new topic for the mobile industry and is currently moving from the drawing board to reality with many trials planned for later this year. The global groups, including those in China, Japan, South Korea, the USA, and Europe, are trying their best to accomplish the application of millimeter waves for 5G. The key technologies include adaptive beam-forming, antenna arrays, and base stations for unmanned aerial vehicles, e.g., [22].

1) Huawei & Deutsche Telekom (2016.02) & 73 GHz. Experiments achieved multi-user connection speeds up to 70 Gbps, providing the highest mm-wave spectrum efficiency. Moreover, the live demo provided good insights into the advanced multi-beam-forming technology, which could realize an ultra-high broadband experience for customers in indoor scenarios and extremely crowded areas.

2) China Mobile Communications Corporation (CMCC) & Zhongxing Telecommunication Equipment corporation (ZTE) (2016.02) & 15 GHz. The experiment was conducted at 15 GHz with a 500 MHz bandwidth, with SU-MIMO and MU-MIMO peak rates reaching 3.5 Gbps+ and 10 Gbps+, respectively. Moreover, it supports dynamic beam-forming and fast self-adaptive user tracing to realize perfect three-dimensional (3D) coverage.

3) DO Communication Over Mobile Network (DoCoMo) & Ericsson (2016.02) & 15 GHz. DoCoMo and Ericsson conducted a joint 5G technologies trial, which achieved cumulative data throughput of

20 Gbps in an outdoor environment at the 15 GHz frequency band with two simultaneously connected mobile devices [23].

4) Google (2016.02) & 28 GHz. Google plants to complete its solar-powered unmanned aerial vehicles base station in the millimeter wave band to provide high-speed connectivity across the globe. The company is experimenting with focused transmission from a phased array in an attempt to achieve their goal.

5) South Korean (SK) Telecom & Samsung (2016.03) & 28 GHz. SK Telecom announced one of the first cases confirming the use of millimeter wave technology, which was tested in both network and outdoor environments and verified the performance of a 5G system in the 28 GHz band, in cooperation with Samsung. The results of the tests will contribute to building a pilot 5G network for testing later this year.

6) T-Mobile (2016.03) & 39 GHz. T-Mobile has submitted an application to FCC and plan to conduct four millimeter-wave trials at 39 GHz in indoor and outdoor scenarios.

7) Qualcomm (2016.10) & 28 GHz. Qualcomm has been planning a millimeter wave base station in which the designed antenna prototype had 128 antenna elements with 16 controllable RF channels. The device contains four selectable sub-arrays, each with four controllable RF channels. Moreover, directional beam-forming can be used to ensure stable performance of the equipment.

8) NYU WIRELESS (2016.10) & 73 GHz. Rappaport and his team conducted a measurement campaign in a rural town in the southwestern part of the state, using the 73 GHz mm-wave frequency band [24]. They discovered that, for less than 1 watt of power and using 27 dBi antennas, they were still able to achieve a reasonable signal strength over 10 km.

9) DoCoMo & 28 GHz. This experimental trial is intend to evaluate the feasibility of using the 28 GHz band with super-wide bandwidth of 800 MHz for 5G wireless communication systems. The key technologies include beam-forming, massive MIMO (96x8), spatial multiplexing of multiple data streams, and beam-tracking. We show that higher throughput can be achieved near 1.2 Gbps at many points in an indoor environment. It is also shown that a throughput of over 1 Gbps can be achieved at points around 200 m from the base station in an outdoor LoS environment [25].

10) DoCoMo & Samsung (2016.11) & 28 GHz. DoCoMo completed a 5G trial at 28 GHz with Samsung Electronics and achieved a data speed of more than 2.5 Gbps with a mobile device that was in a vehicle traveling at 150 km/h, thereby demonstrating the feasibility of connectivity for 5G devices in fast-moving trains.

11) DoCoMo & Nokia (2016.11) & 73.5 GHz. DoCoMo and Nokia completed field experiments on the downlink throughput and SNR performance of a 5G millimeter-wave radio access system with beam-forming and beam-tracking in urban environments. The experimental result shows that a maximum throughput of over 2 Gbps is achieved in each of the respective environments. The SNR and throughput performance versus distance from the AP are nearly identical for both environments in LoS scenarios. Furthermore, if reflection paths exist, identical SNR and throughput performance are still achievable in these non-line-of-sight (NLoS) scenarios [26].

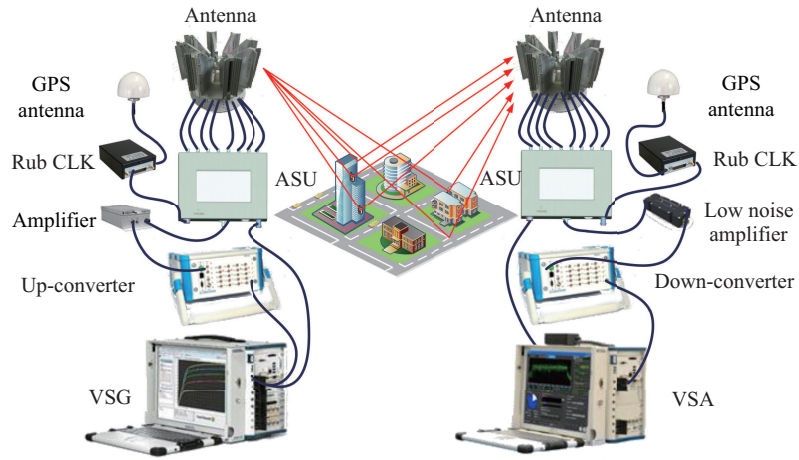
12) Facebook (2016.11) & 60–90 GHz. Facebook demonstrated a data rate of 20 Gbps over 13 km with millimeter-wave technology in peer-to-peer (P2P) millimeter wave trials in remote areas of Southern California at radio frequencies from approximately 60 GHz to 90 GHz with a transmission bandwidth of 2 GHz.

## 4 Two aspects of 6–100 GHz research

### 4.1 Channel measurement hardware

#### 4.1.1 High-frequency channel measurement platforms

One popular way to achieve the channel propagation characteristics is to performance measurements on the channel. However, the measurement capability and accuracy are determined by the designed plat-

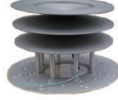
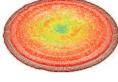

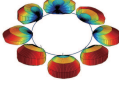


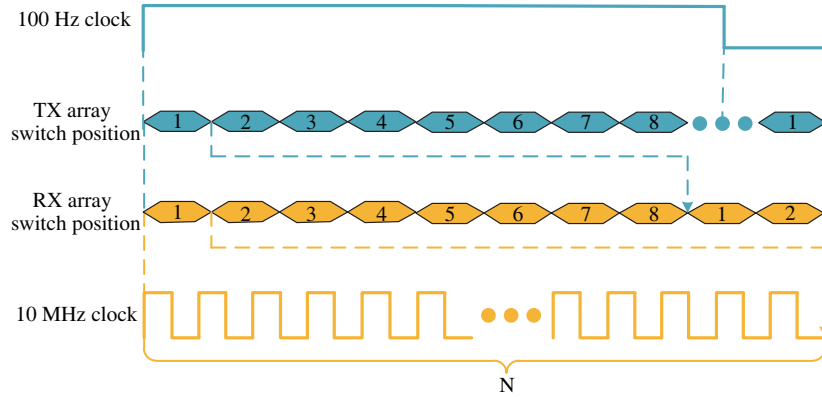
**Figure 2** Structure of the channel measurement platforms.

form. To the best of our knowledge, the prober sounder built by Elektrobit is a very popular channel measurement platform for low frequencies, and it has excellent abilities to realize time synchronization and conduct MIMO measurements. However, because of the limitation of the converter, this platform can only measure channels below 6 GHz. In addition, its maximum available bandwidth is only 200 MHz, which cannot meet the need of a 5G communication system. For high-frequency bands, the measurement platform should have large system bandwidth together with the ability to transmit high-frequency signals. Currently, there are mainly two kinds of high-frequency channel measurement platforms: a) VNA-based; b) discrete component (DC)-based. The main difference between them is that for the VNA-based sounder, the TX and RX are connected via cables as a whole whereas the DC-based sounder consists of several components, e.g., the converter and the amplifier. Obviously, in the case of the latter, the specific components of the platform can vary considerably but they have a similar function. More importantly, the structure of this kind of platform is similar. The platform shown in Figure 2 is set up by BUPT, for example, a pair of 8-horn antenna arrays is deployed, which supports omnidirectional MIMO measurement. Specifically, the operation procedures are as follows: at the TX side, modulated specific pseudo-noise (PN) code is generated by the PN sequence generator. Then, it is modulated to the corresponding high frequency after up-conversion. An amplifier is used to increase the signal power up to 30 dBm before proceeding through the antenna switch unit (ASU) with eight outputs. In a certain time sequence, the signal is switched to the 8-horn antennas sequentially. Lastly, it is transmitted into the wireless channel by the transmitting antenna. Accordingly, at the RX side, the signal is captured by the 8-horn antennas and then converted to baseband signal after down-conversion. Lastly, the baseband signal will be coherently demodulated using a sliding correlator to acquire the channel impulse response (CIR). Displaying the real-time result helps to determine the validity of the raw measurement data that are eventually stored in the prescribed format for post-processing.

In addition, antennas are also quite important when conducting measurements. Table 1 contains details of two kinds of antennas: the biconical antenna and the 8-horn array antenna. We can see that both of them have high gain, which can be used to compensate for the large path loss. Moreover, they are both omnidirectional on the azimuth domain to enable them to receive more multiple paths from different directions than directional antennas. Especially, the 8-horn array antenna can be used to conduct MIMO measurements by connecting the ASU. Time synchronization between the TX and RX is required to enable this ASU to function normally. This platform uses a pair of rubidium clocks with an optional integrated global positioning system (GPS) receiver, which disciplines the GPS reference at 1-ns resolution. After synchronizing with the GPS reference, each rubidium clock provides the ASU with a clock source of 10 MHz to control the switching sequence. Then, two 100-Hz clock sources are generated by a National Instruments (NI) board-6683, which can also use the GPS signal as reference to control the start of switching. A detailed timing diagram is shown in Figure 3. We can see that both the 100-Hz

**Table 1** Biconical antenna and 8-horn array antennas

Ant. entity/pattern				
Ant. Type	Biconical		8-horn array	
Ant. Gain	12.5 dBi		21.5 dBi (each)	
H-HPBW	360°		360°	
E-HPBW	5°		5°	

**Figure 3** Timing diagram of the MIMO measurement platform.

clock and the 10-MHz clock play vital roles when the ASUs switch in order. In terms of the 100 Hz clock, the ASUs will reset and begin to switch when the rising edge of the clock signal arrives. The 10-MHz clock provides the time unit for each sub-channel. For example, the duration of the sub-channel in Figure 3 is  $N \times 100$  ns. Generally, although the clock sources between the TX and RX are aligned with GPS, there may be a time difference. Hence, it is necessary to transmit more than one PN sequence in each sub-channel to ensure that a completed PN sequence will be received without the effects of the time difference.

VNA is used as the key equipment in the VNA-based channel measurement platform. The equipment is connected to both the TX and RX antennas. Obviously, the selection of the measurement frequency and bandwidth is accomplished inside the VNA. Since the VNA can only measure the channel transfer function in the frequency domain, an inverse fast Fourier transform (IFFT) should be conducted to obtain the CIR in the time domain during data post-processing after the measurement. The advantage of this method is that its self-synchronization and setup are relatively simple. Furthermore, the measurement frequency and bandwidth are also flexible. The disadvantage of this method lies in its limited measurement distance since cables have to be used to connect the TX and RX antennas to the corresponding transmitting and receiving ports on the VNA. In contrast, in the DC-based method, the TX and the RX are symmetric but separate. Therefore, the measurement distance is not limited. In addition, this measurement platform framework provides a good reference for other research institutes or companies planning to build a MIMO measurement platform and this also partly promotes the development of future 5G wireless communication.

#### 4.1.2 Effects of antennas on measurements

As is well known to us, the antenna is a key component in the channel measurement campaign. In this respect, an omnidirectional antenna, such as a dipole antenna, could obtain a greater variety of channel information under the same conditions compared with the directional antenna, such as a horn antenna. To explain this problem persuasively, we conducted a series of indoor office channel measurements at 14 GHz with a pair of horn antennas and a pair of dipole antennas [27]. During the measurements, the



**Table 2** Comparing the PDP obtained by different kinds of antenna

Case	Path number	RMS delay spread (ns)		Mean MED (ns)
		90% CDF	Mean	
Horn	6	30	21	53
Dipole	9	52	33	128

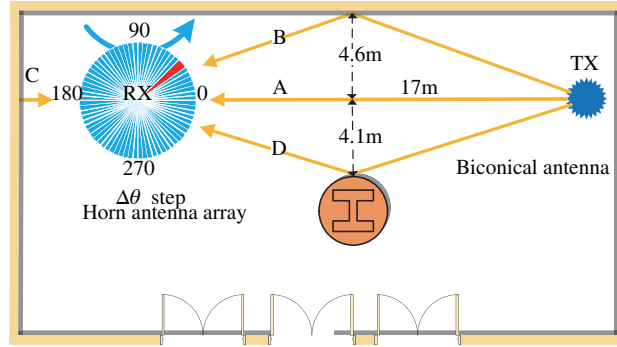
two kinds of antenna configurations were used separately at the same LoS measured locations. We mainly compared the power delay profile (PDP) and analyzed the path number, the root mean square (RMS) delay spread (DS), and the maximum excess delay (MED). Table 2 summarizes the analysis results.

The results in this table indicate that the dipole antenna can receive three additional multiple paths compared to the horn antenna, which is the same as the expectation. Although the dipole antenna has a low antenna gain, it can detect across a larger space range. Especially, it can receive a large number of reflected multiple paths from the rear side. In terms of the horn antenna, most of the energy is transmitted in one direction, which results in high gain but small half-power beam width (HPBW). In addition, the multiple paths received by the horn antenna will be more similar, especially under LoS conditions. The analysis results on the delay domain also support the above-mentioned opinions. We can see that the mean of the RMS DS is 33 ns when using the dipole antenna, which is 12 ns more than when using the horn antenna. In addition, the MED result shows the same trend. Hence, these two kinds of antenna can obtain different channel characteristics. Considering the application of the channel model, it is easier to apply a model based on omnidirectional antenna measurements to different scenarios. In cellular systems, the antenna at the UE side is generally omnidirectional; However, the high path loss in the high-frequency band needs to be compensated for by using a horn antenna with high gain. In particular, high antenna gain is essential when conducting measurements in NLoS scenarios. These two aspects are balanced by adopting a method of virtual measurements, which is realized by rotating the horn antenna. The next section discusses this method in detail.

#### 4.1.3 Effects of the rotation step on virtual measurements

Currently, virtual MIMO measurements are applied prevalently to obtain the spatial characteristics of a channel. The measurements involve setting up the virtual multi-element circular array by rotating a horn antenna to transmit or receive an omni-directional signal, which can characterize the channel more exactly. Moreover, high-gain steerable antennas can be utilized to compensate for the large propagation attenuation in the link budget. Theoretical discussion indicates that the virtual MIMO measurement is similar to the real MIMO measurement based on the platform, as shown in Figure 2, and they both use the time division theory to enable the antenna to acquire signal energy at different times. In addition, a method for analyzing the virtual MIMO measurement results also needs to be researched. The SAGE algorithm, which has been extensively applied to estimate the channel parameters, e.g., the delay, power azimuth spectrum (PAS), and Doppler frequency, based on the MIMO measurement results, is an extension of the expectation-maximization (EM) algorithm.

However, considering the ambiguity of the rotating step and the HPBW of the directional antenna, it is necessary to pay attention to the effects of the size of the virtual array on the precision of the estimated results in the virtual MIMO measurement. This effect was investigated by conducting a virtual measurement in a typical indoor LoS scenario of BUPT with a biconical antenna at the TX side and a horn antenna at the RX side [28]. The horn antenna has the same HPBW of  $10^\circ$  in both the azimuth and the elevation dimensions [29]. In the measurement, the horn antenna is rotated from  $0^\circ$  to  $360^\circ - \Delta\theta$  with a rotating step of  $\Delta\theta$  in the azimuth dimensions, where  $\Delta\theta = 2^\circ, 3^\circ, 5^\circ, 8^\circ, 10^\circ$ , such that the adjacent rotations have different visual overlap as shown in Figure 4. Empirically, this measurement can be regarded as a  $1 \times (360/\Delta\theta)$  MIMO channel measurement. Then, the SAGE algorithm was utilized to extract the channel spatial characteristics to verify whether this algorithm would be as effective as expected. Figure 5 presents the results of PAS at each rotating step. In order to compare the distribution of multipath components (MPCs), the PAS in the dynamic ranges of 35 dB and 20 dB are presented,



**Figure 4** Layout of the virtual MIMO measurement scenario.

**Table 3** Comparison of time cost and the number of multipaths in the azimuth domain. DR denotes the dynamic range below the peak power in PAS and L is the initialized total number of MPCs in the estimation procedure using the SAGE algorithm

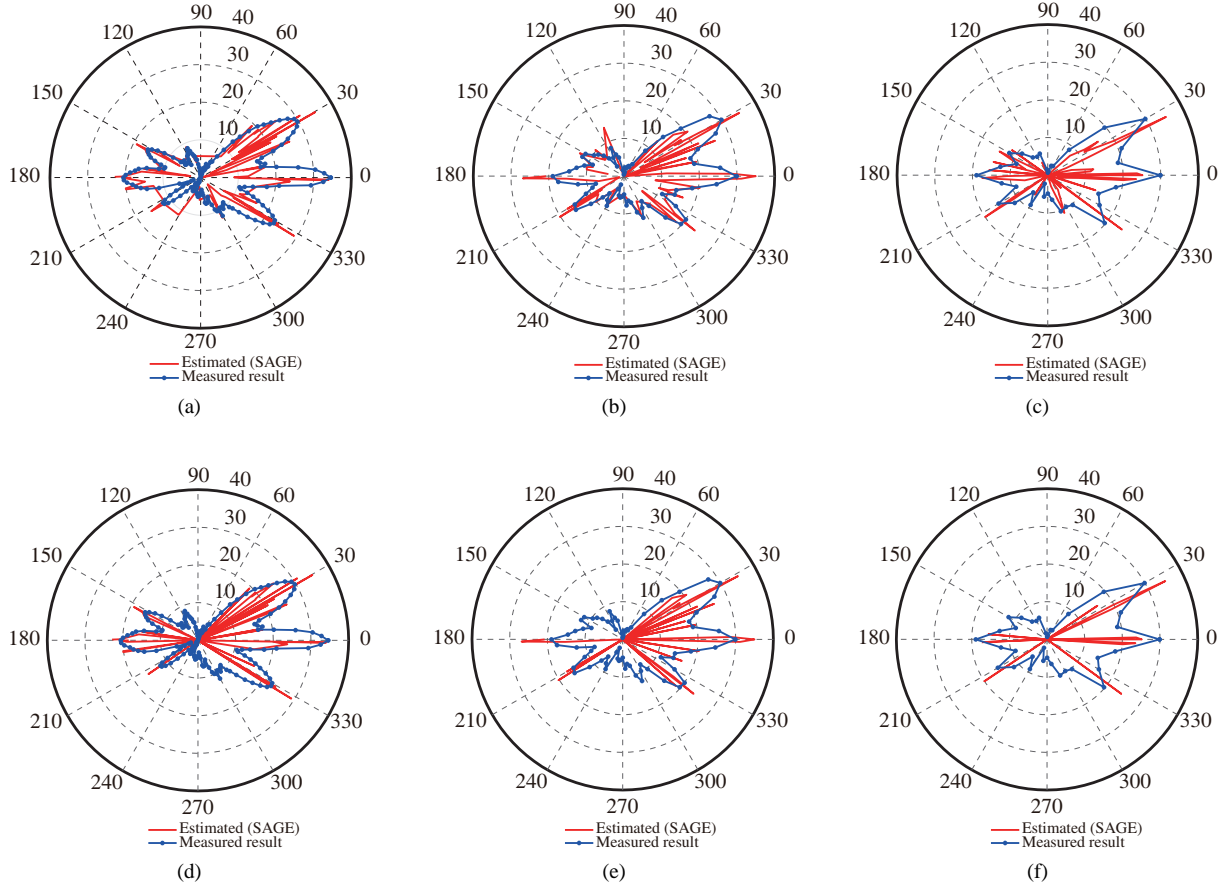
Rotate step	Data acquisition time (min)	Estimation time by SAGE (min)	Estimated MPCs by SAGE ( $L = 100$ )				
			DR = 35 dB	DR = 30 dB	DR = 25 dB	DR = 20 dB	DR = 15 dB
2°	30	120	91	86	65	44	22
3°	20	105	85	81	63	41	22
5°	12	80	60	54	38	23	13
8°	9	70	59	45	33	24	12
10°	6	60	44	32	25	12	6

**Table 4** Comparison of RMS angle spread

Rotating step	$\mu_{\lg \text{ASA}} \lg \text{ASA} = \lg(\text{ASA}/1^\circ)$
2°	1.67
3°	1.65
5°	1.57
8°	1.45
10°	1.34
3GPP (Indoor, LoS)	1.58

respectively. The red line is the estimated PAS using the SAGE algorithm whereas each blue dot shows the received power level at each rotating angle bin and the blue line is the envelope, representing the synthesized result based on the measurement. As we can see from the envelope, the four main propagation routes (lobes) have a significant received power level. One is at 0° azimuth direction, corresponding to the LoS direction. The remaining directions are the 30°, 180°, and 330° azimuth directions, respectively, which belong to high-reflective directions from walls or pillars. The situation agrees well with the real scenario in Figure 4. However, in view of the distribution of the estimated PAS at each rotating step, the consistency with the real scenario differs significantly. The MPCs at the step of 2° are the most, followed by those at the step of 5°, with those at the step of 10° being the least. Table 3 presents the exact results, including the time cost during the rotation measurement and the processing procedure of the SAGE algorithm. In addition, the RMS angle spread is a key parameter to characterize the dispersion of MPCs in the spatial domain. Table 4 presents the results of the RMS azimuth spread of the arrival angles (ASA). The results in Table 4 indicate the average value of ASA displays a decreasing trend as the size of the rotating step is enlarged.

Overall, the experimental analysis revealed that the SAGE algorithm is still available to extract the channel spatial information from virtual MIMO measurement results. However, it is intuitive to show that the size of the rotating step has a significant effect on the precision of the estimated results using



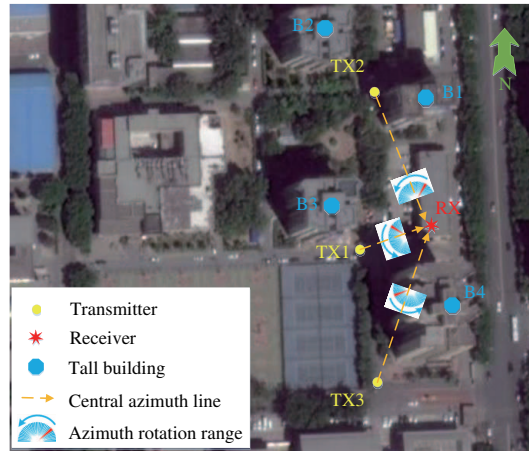
**Figure 5** Results of PAS comparison. The red line is the estimated PAS using SAGE algorithm whereas each blue dot shows the received power level at each rotating angle bin and the blue line is the synthesis envelope based on measurements. (a) PAS-35 dB-2°; (b) PAS-35 dB-5°; (c) PAS-35 dB-10°; (d) PAS-20 dB-2°; (e) PAS-20 dB-5°; (f) PAS-20 dB-10°.

the SAGE algorithm. Moreover, because the horn antenna is rotated artificially rather than using an ASU with a high switching speed of tens of nanoseconds, the virtual MIMO measurement is quite time consuming, and the smaller rotating step leads to greater time cost. Since the static channel environment is necessary for further data processing when rotating the horn antenna, which may easily be reached indoors whereas walking people and moving vehicles present a great challenge for conducting virtual MIMO measurements in outdoor environments. Therefore, the rotating step is a key factor we must take into consideration in the virtual MIMO measurement.

## 4.2 Channel parameter analysis

### 4.2.1 SAGE in a virtual MIMO measurement

Similar to the virtual measurement mentioned above, recently, a large number of virtual MIMO measurements have been conducted in the millimeter wave band in typical indoor or outdoor environments to analyze the channel spatial characteristics using the SAGE algorithm. In order to further demonstrate whether the SAGE algorithm is capable of analyzing results obtained by virtual MIMO measurements, a virtual measurement was conducted in a typical Urban Micro (UMi) scenario [30]. The RX was located in the rooftop (13.38 m above the ground), and the TX with a biconical antenna (2 dBi, 360° and 40° HPBW in azimuth and elevation, respectively) had three alternative positions (TX1, TX2, and TX3) at a height of 1.66 m above the ground. On the RX side, a 25-dBi horn antenna (11° and 10° HPBW in azimuth and elevation, respectively) was rotated by 180° with a step of 5° in the azimuth domain and pointed to three adjacent different elevation angles with an increment of 10°. The exact scenario is shown



**Figure 6** Layout of measurement environment. TX1 and TX3 are located in LoS and NLoS positions, respectively. TX2 corresponds to the junction position. The east and the horizon plane are the reference directions at  $0^\circ$  in azimuth and elevation, respectively.

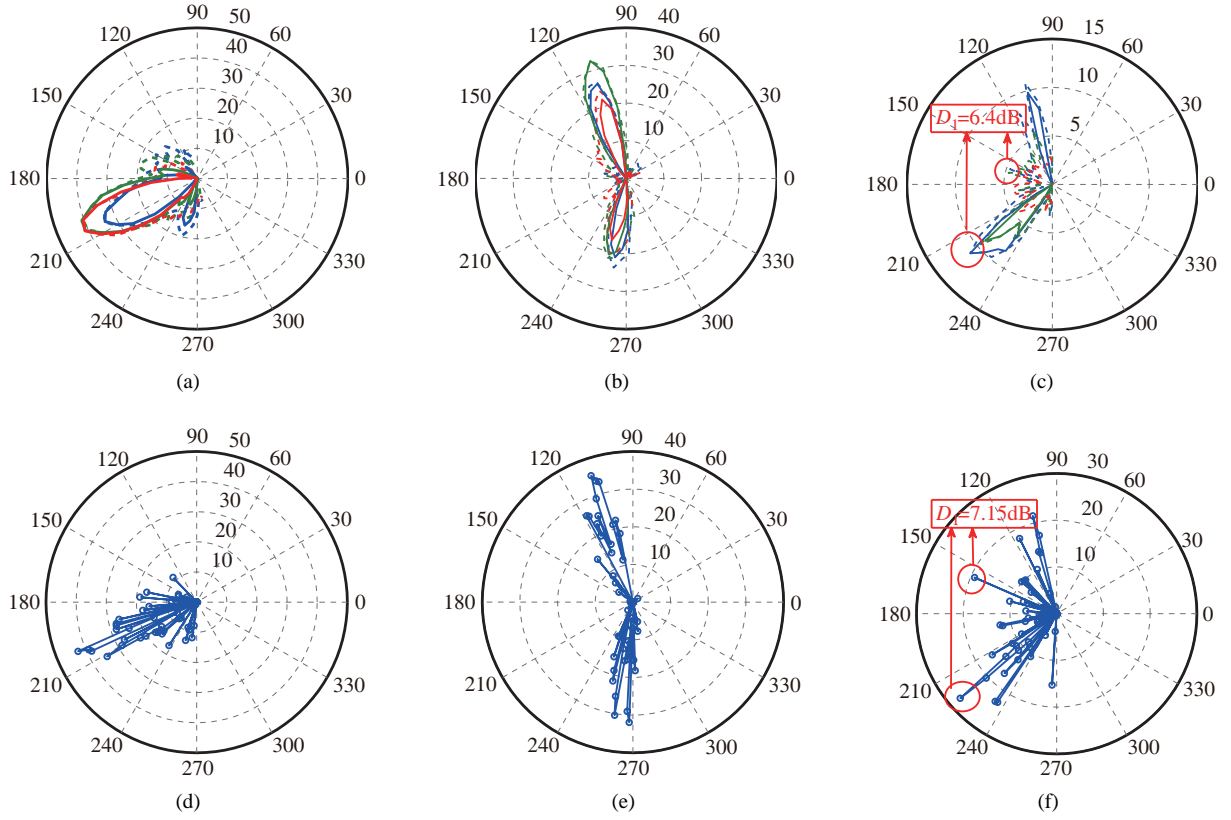
in detail in Figure 6.

After the CIRs were recorded at each pointing angle, two methods were adopted to resolve the MPCs in the space domain. The first involved directly obtaining angle parameters by using the raw data at each bore-sight angle of the horn antenna. The other was to extract the MPCs using the SAGE algorithm. Figure 7 presents the comparison result on PAS of the RX corresponding to each TX. The dashed lines represent the PAS from RD, termed the original result, whereas the solid lines show the PAS restructured from the SAGE results. Here it should be noted that the angle information of the three circles is shown in the PAS because three elevation angles were used during rotation. Figure 7 represents the PAS result of the RX with TX in LoS, junction, and NLoS scenarios, respectively. In the LoS scenario, there is a strong lobe in the PAS because of the shorter distance and obvious LoS multipath. On the other hand, the lack of a LoS multipath results in the lobes in the PAS originating from the reflection multipath as a consequence of tall buildings when the TX is located in a NLoS or junction environment. In addition, in terms of a comparison between the original PAS and restructured PAS, there is significant consistency between the results obtained by using these two methods regardless of whether they are used under LoS or NLoS conditions. Therefore, considering the distribution of PAS, it is found that the SAGE algorithm also performs well for extracting spatial parameters in virtual MIMO measurements. Especially, when observing the situation shown in Figure 5, the dynamic range of the original PAS calculated by raw data is smaller than that using the SAGE algorithm. This can be explained by keeping in mind that more tiny paths with weak power are estimated using the SAGE algorithm, thereby enlarging the dynamic range of PASs. The above investigations are also proven by the results shown in Figure 5. In comparison with the small amount of variation in the power difference the dynamic range changes sharply in these two methods. This illustrates the good performance of the SAGE algorithm.

#### 4.2.2 Estimation of the $K$ -factor based on fixed-point measurements

In the radio wave propagation channel, since there are obstructions and specular surfaces, the TX signals reach the RX along different paths. In addition, the superposition of these multiple paths contributes to channel fading. Generally, the distribution of channel fading below 6 GHz is regarded as Ricean in a LoS scenario and Rayleigh in a NLoS scenario [31]. As the frequency increases, the propagation characteristics of the radio wave change and it is known that a radio wave with higher frequency exhibits relatively weak diffraction. This is also the reason why the dominant propagation mechanisms of radio waves change [32]. Hence, it is necessary to research the  $K$ -factor statistics in the high-frequency band.

Due to the limits of the measurement platform, most of the measurements were conducted without mobility [33,34]. Hence, it is necessary to extract the  $K$ -factor from the fixed-measurement data. When the user equipment (UE) remains fixed at each measured location, i.e., measurements are conducted in



**Figure 7** Comparison of PAS by RD and SAGE in the azimuth. Original PAS vs. restructured PAS at (a) TX1; (b) TX2; (c) TX3; PAS from SAGE at (d) TX1; (e) TX2; (f) TX3.

the absence of mobility, then the variations among the different temporal samples of the impulse response are only attributable to noise and inadvertent movements of surrounding people rather than to different channel realizations due to phase changes between the MPCs. However, in the frequency domain, there are different narrowband channel realizations at the different frequency positions, and thus the Ricean factor can be extracted from the ensemble of these realizations. The mathematical description of this process is as follows:

$$H(t; f) = \int_{\tau} h(t; \tau) \exp(-j2\pi f\tau) d\tau, \quad (1)$$

where  $h(t; \tau)$  is the channel impulse response (CIR) and  $\tau$  is the delay. For the channel frequency response (CFR),  $H(t; f)$ , we can write

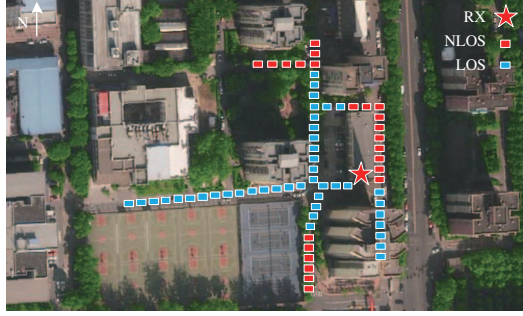
$$H_i = \sqrt{\frac{K}{K+1}} + \sqrt{\frac{1}{K+1}} g'_i, \quad i = 1, 2, \dots, n, \quad (2)$$

where  $H_i$  is the  $i$ th CFR,  $n$  is the number of frequency positions,  $g_i$  is a complex zero-mean Gaussian process in the frequency domain, and  $K$  is the Ricean factor. Then, we use the moment-method to calculate the narrow band K-factor [19] for its simplicity as follows:

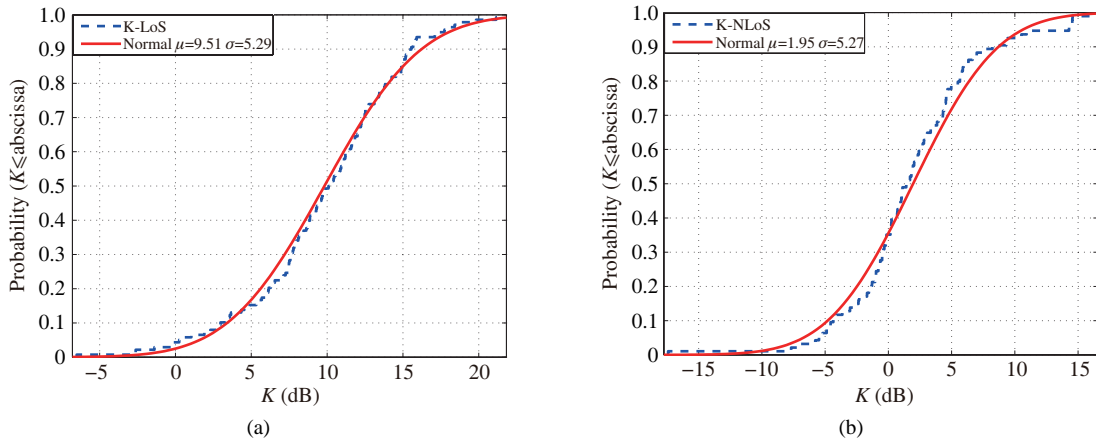
$$G_a = \frac{1}{n} \sum_{i=1}^n |H_i|^2, \quad (3)$$

$$G_v = \frac{1}{n-1} \left( \sum_{i=1}^n |H_i|^4 - nG_a^2 \right), \quad (4)$$

$$\hat{K} = \frac{\sqrt{G_a^2 - G_v}}{G_a - \sqrt{G_a^2 - G_v}}, \quad (5)$$



**Figure 8** Measurement layout in the UMi scenario at 28 GHz.



**Figure 9** K-factor statistics under LoS and NLoS conditions, respectively. (a) LoS scenario; (b) NLoS scenario.

where  $\hat{K}$  is the estimation of the K-factor,  $G_a$  and  $G_v$  are the second and fourth moments of the envelope of CFR.

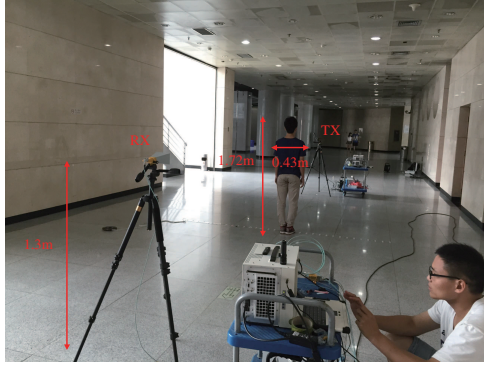
To obtain the distribution of the high-frequency channel fading, we conducted a measurement with mobility in a UMi scenario at 28 GHz [30, 35]. In this scenario, a sectored antenna and an omnidirectional antenna were used to collect the multiple paths. Figure 8 shows the layout that was used during measurements, during which the TX was mounted on the trolley and fixed on the ground. The spacing between the successive measured spots was 2 m.

We applied the moment-method to calculate the K-factor in the frequency domain to obtain the K-factor statistics shown in Figure 9. We can see that the K-factor (in dB) of both the LoS and NLoS scenarios approximately displays a normal (Gaussian) distribution. In the LoS scenario, the mean value of the fitted normal distribution is 9.51 dB, which is a little larger than the experimental results, i.e., 9 dB, as obtained in [4]. The difference in the measured environment was mainly responsible for the different results. In the NLoS scenario, the mean value of the fitted normal curve is 1.95 dB, which suggests Ricean fading rather than Rayleigh fading. This is mainly because of the existence of a dominant and stable component due to the reflections; similar effects have been observed previously below 6 GHz [36].

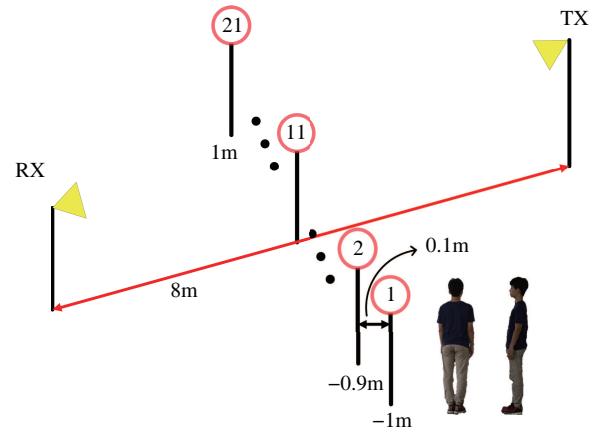
#### 4.2.3 Blockage of human body

According to the Friis free space path loss formula, it is known widely that the millimeter wave has large propagation attenuation. Additionally, wireless transmission is susceptible to shadowing loss resulting from blockage of the LoS path by the human body. This further influences the utilization of directional antennas to overcome the large path loss in the propagation link [37, 38]. Therefore, a greater understanding of human body shadowing (HBS) is required for the design and deployment of a mm-wave communication system.

The influence of HBS was researched by performing a measurement campaign in a typical indoor shopping mall scenario at 28 GHz [39], as shown in Figure 10. The results provide a simple model for



**Figure 10** Measurement environment and setup for 28 GHz HBS.



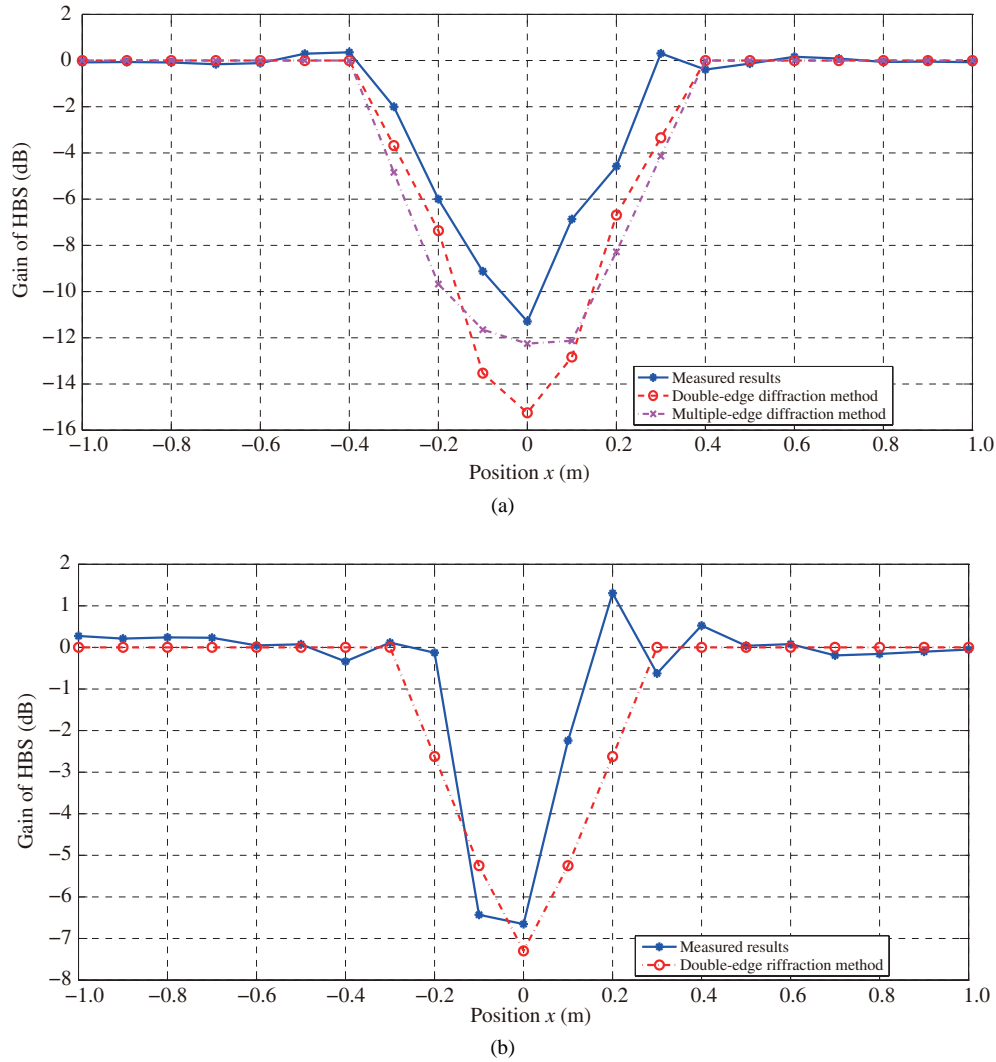
**Figure 11** Schematic diagram of the measurement scenario. Person moves perpendicularly to LoS path with human body facing either towards TX or perpendicularly to LoS path.

predicting and analyzing the effect of HBS based on a special case at 28 GHz. In the measurement, a typical case of blocking by a human body was adopted to validate the HBS model and acquire a comprehensive HBS profile. The specific details are presented in Figure 11. Then, during further data processing, two methods of double-edge diffraction and multiple-edge diffraction are utilized to analyze the characteristics of HBS, and these two methods and the measured result were compared.

As shown in Figure 11, in order to study the influence of the direction of the human body and emulate person crossing the LoS path, the person crossed the LoS path vertically at the midpoint of TX and RX, with the body either facing TX or perpendicular to the LoS path, respectively. The results are presented in Figure 12 and it is clear that the measured results are in good correspondence with the results of these two models. This illustrates that the received signal is mainly due to diffraction from the vertical edges of the human body. In addition, with the person facing towards TX, the result of the double-edge diffraction method is 3.96 dB smaller than the measured result compared to the multiple-edge of 0.96 dB [40, 41]. These results are mainly attributed to the failure of the diffraction ray to reach the RX because the ray was obstructed by the person's shoulder. Therefore, in this case, the multiple-edge diffraction method is simplified as the double-edge diffraction method. In terms of the shadowing width (SW), which is defined as the width of the area where the shadowing gain is below 0 dB, the SW value of the measured results are 0.8 m and 0.4 m in the two cases, respectively. This result can be well explained when considering that the former has a relatively larger shadowing area compared with the latter.

## 5 Conclusion

The use of the high-frequency spectrum in mobile communications as one of the solutions to meet the exploratory demand of mobile data services has attracted increasing attention. This paper provided a detailed description of the potential high-frequency bands in the world and illustrated that negotiation is essential to enable various countries and regions to reach consensus about the allocation of high-frequency bands for future 5G communication. We next presented an overview of chip development and field trials in the millimeter-wave band. It became clear that many companies in the world were contributing to the trial to promote the development of 5G key technologies and support global unified 5G standardization. Research results were presented in respect of two aspects of channels: channel measurement hardware and channel parameter analysis. In terms of channel measurement hardware, we showed the framework of a MIMO channel measurement platform and provided a detailed description of the time synchronization scheme, which provides a reference for building a channel measurement platform. Furthermore, an omnidirectional antenna was shown capable of capturing more multipath components and obtaining a larger delay spread than a directional antenna. This means that when



**Figure 12** Human body moves perpendicularly to the LoS path. (a) Human body faced towards TX; (b) human body faced perpendicularly to LoS path.

applying beam-forming technology, smaller delay spread and less inter-symbol interference tends to be obtained. In our virtual measurements, we found that decreasing the size of the rotating step could increase the precision of the parameters estimated using the SAGE algorithm correspondingly, which suggests a smaller rotating step to obtain more exact channel information. In terms of the analysis of channel parameters, the performance of the SAGE algorithm to extract angle information from virtual measured data was demonstrated. Considering the popularity of virtual measurements obtained by rotating directive antennas when researching the channel characteristics for the high-frequency band, the SAGE algorithm can be a reliable method for characterizing the channel. Furthermore, a method for extracting the K-factor from fixed-point measured data was introduced; thus, when incorporating mobility in measurements it is not necessary to obtain statistics of the K-factor in a channel, and we can estimate the K-factor for temporal fading based on the analysis of frequency selectivity. Blockage by the human body was also analyzed based on real-world measurements and we found that it could be modeled with the double-edge model and multiple-edge diffraction models. Considering the channel properties of the 6–100 GHz band and its application requirements, a deterministic model that utilizes the map information has recently become attractive recently. These results provide references to further high-frequency channel research.



**Acknowledgements** The work was supported by National Natural Science Foundation of China (Grant No. 61322110), National Science and Technology Major Project of the Ministry of Science and Technology (Grant No. 2015ZX03002008), National High-tech R&D Program of China (863) (Grant No. 2015AA01A703), and Doctoral Fund of the Ministry of Education (Grant No. 20130005110001). The measurement platform was partially funded by SAMSUNG, and the data collections were funded by ZTE, Huawei, and CMCC.

**Conflict of interest** The authors declare that they have no conflict of interest.

## References

- 1 ITU-R. IMT vision-framework and overall objectives of the future development of IMT for 2020 and beyond 6–100. ITU-R. WP5D TD-0625, 2015
- 2 You X H, Pan Z W, Gao X Q, et al. The 5G mobile communication: the development trends and its emerging key techniques (in Chinese). *Sci Sin Inform*, 2014, 44: 551–563
- 3 Belbase K, Kim M, Takada J, et al. Study of propagation mechanisms and identification of scattering objects in indoor multipath channels at 11 GHz. In: *Proceedings of 9th European Conference on Antennas and Propagation (EuCAP)*, Lisbon, 2015. 1–4
- 4 3GPP. Channel model for frequency spectrum above 6 GHz 6–100. 3GPP TR 38.900, 2016
- 5 ITU-R Rec. Specific attenuation model for rain for use in prediction methods. P.838-3. 2005
- 6 ITU-R Rec. Attenuation by atmospheric gases. P.676-8. 2009
- 7 Zhang J H, Tang P, Tian L. The current and future of high frequency channel modeling. *Telecommun Netw Technol*, 2016, 3: 10–17
- 8 Kyro M, Ranvier S, Kolmonen V M, et al. Long range wideband channel measurements at 81–86 GHz frequency range. In: *Proceedings of 4th European Conference on Antennas and Propagation (EuCAP)*, Barcelona, 2010. 1–5
- 9 Rappaport T S, Sun S, Mayzus R, et al. Millimeter wave mobile communications for 5G cellular: it will work! *IEEE Access*, 2013, 1: 335–349
- 10 Rappaport T S, Murdock J N, Gutierrez F. State of the art in 60 GHz integrated circuits and systems for wireless communications. *Proc IEEE*, 2011, 99: 1390–1436
- 11 Sato K, Manabe T, Ihara T, et al. Measurements of reflection and transmission characteristics of interior structures of office building in the 60 GHz band. *IEEE Trans Antenn Propag*, 1997, 45: 1783–1792
- 12 Lei M Y, Zhang J H, Tian L. 28 GHz indoor channel measurements and analysis of propagation characteristics. In: *Proceedings of the International Symposium on Personal, Indoor and Mobile Radio Communications (PIMRC)*, Washington DC, 2014. 208–212
- 13 Wang H M, Hong W, Chen J X, et al. IEEE 802.11 aj (45GHz): a new very high throughput millimeter-wave WLAN System. *China Commun*, 2014, 11: 51–62
- 14 Samimi M K, Rappaport T S. 3-D millimeter-wave statistical channel model for 5G wireless system design. *IEEE Trans Microw Theory Tech*, 2016, 64: 2207–2225
- 15 Hur S, Cho Y J, Lee J, et al. Synchronous channel sounder using horn antenna and indoor measurements on 28 GHz. In: *Proceedings of the International Black Sea Conference on Communications and Networking (BlackSeaCom)*, Odessa, 2014. 83–87
- 16 Cheng X, Yu B, Yang L Q, et al. Communication in the real world: 3D MIMO. *IEEE Wirel Commun Mag*, 2014, 21: 136–144
- 17 Rappaport T S, Maccartney G R, Samimi M K, et al. Wideband millimeter-wave propagation measurements and channel models for future wireless communication system design. *IEEE Wirel Commun*, 2015, 63: 3029–3056
- 18 Molisch A F. *Wireless Communications*. 2nd ed. Chichester: John Wiley & Sons Ltd., 2011
- 19 Greenstein L J, Michelson D G, Erceg V. Moment-method estimation of the ricean k-factor. *IEEE Commun Lett*, 1999, 3: 175–176
- 20 Zhang J H. The interdisciplinary research of big data and wireless channel: a cluster-nuclei based channel model. *China Commun*, 2016, 13: 14–26
- 21 European Commission. Opinion on spectrum related aspects for next-generation wireless systems (5G). RSPG16-032 FINAL. 2016
- 22 Gozalvez J. 5G worldwide developments [mobile radio]. *IEEE Veh Technol Mag*, 2017, 12: 4–11
- 23 NTT DOCOMO. Technical specification group radio access network: 5G trials with major global vendors. *NTT DOCOMO Technical Journal*, 2016, 17: 60–69
- 24 Maccartney G R, Sun S, Rappaport T S, et al. Millimeter wave wireless communications: new results for rural connectivity. In: *Proceedings of the 5th Workshop on All Things Cellular: Operations, Applications and Challenges*, New York, 2016. 31–36
- 25 Obara T, Okuyama T, Inoue Y, et al. Experimental trial of 5G super wideband wireless systems using massive MIMO beamforming and beam tracking control in 28 GHz band. *IEICE Trans Commun*, 2017, E100-B, doi: 10.1587/transcom.2016FGP0020
- 26 Inoue Y, Yoshioka S, Kepler J. Field experimental trials for 5G mobile communication system using 70 GHz-band. In: *Proceedings of the IEEE Wireless Communications and Networking Conference Workshops (WCNCW)*, San Francisco,

2017. 1–6
- 27 Miao R Q, Tian L, Zheng Y, et al. Indoor office channel measurements and analysis of propagation characteristics at 14 GHz. In: Proceedings of the Personal, Indoor, and Mobile Radio Communications (PIMRC), Hong Kong, 2015. 2199–2203
  - 28 Hu Z X, Tian L, Tang P, et al. The effects of the rotating step on analyzing the virtual MIMO measurement results at 28 GHz. In: Proceedings of the IEEE Vehicular Technology Conference (VTC-Fall), Toronto, 2017. 1–5
  - 29 Gao X X, Tian L, Tang P, et al. Channel characteristics analysis of angle and clustering in indoor office environment at 28 GHz. In: Proceedings of the IEEE Vehicular Technology Conference (VTC-Fall), Montreal, 2016. 1–5
  - 30 Tang P, Tian L, Zhang J H. Analysis of the millimeter wave channel characteristics for urban micro-cell mobile communication scenario. In: Proceedings of 11th European Conference on Antennas and Propagation (EuCAP), Paris, 2017. 2880–2884
  - 31 Stuber G L. Principles of Mobile Communication. 3rd ed. New York: Springer Science & Business Media Publishing, 2011
  - 32 Belbase K, Kim M, Takada J I. Study of propagation mechanisms and identification of scattering objects in indoor multipath channels at 11 GHz. In: Proceedings of 9th European Conference on Antennas and Propagation (EuCAP), Lisbon, 2015. 1–4
  - 33 Liou A E N, Huang H H H, Michelson D G. Issues in the estimation of ricean k-factor from correlated samples. In: Proceedings of the IEEE Vehicular Technology Conference (VTC-Fall), Montreal, 2006. 1–4
  - 34 Lee J, Liang J Y, Park J J, et al. Directional path loss characteristics of large indoor environments with 28 GHz measurements. In: Proceedings of the Personal, Indoor, and Mobile Radio Communications (PIMRC), Hong Kong, 2015. 2204–2208
  - 35 Tang P, Zhang J H, Molisch A F, et al. Estimation of the ricean k-factor for wideband channel fading. *IEEE Trans Antenn Propag*, 2017. Submitted
  - 36 Molisch A F, Asplund H, Heddergott R, et al. The COST259 directional channel model-part I: overview and methodology. *IEEE Trans Wirel Commun*, 2006, 5: 3421–3433
  - 37 Karadimas P, Allen B, Smith P. Human body shadowing characterization for 60-GHz indoor short-range wireless links. *IEEE Antenn Wirel Propag Lett*, 2013, 12: 1650–1653
  - 38 Manabe T, Miura Y, Ihara T. Effects of antenna directivity and polarization on indoor multipath propagation characteristics at 60 GHz. *IEEE J Sel Areas Commun*, 1996, 14: 441–448
  - 39 Chen X B, Tian L, Tang P, et al. Modelling of human body shadowing based on 28 GHz measurement results. In: Proceedings of the IEEE Vehicular Technology Conference (VTC-Fall), Montreal, 2016. 1–5
  - 40 Kunisch J, Pamp J. Ultra-wideband double vertical knife-edge model for obstruction of a ray by a person. In: Proceedings of the IEEE International Conference on Ultra-Wideband (ICUWB), Hannover, 2008. 2: 17–20
  - 41 Jacob M, Priebe S, Maltsev A, et al. A ray tracing based stochastic human blockage model for the IEEE 802.11ad 60 GHz channel model. In: Proceedings of the 5th European Conference on Antennas and Propagation (EUCAP), Rome, 2011. 3084–3088